Bond–Slip Analytical Formulation toward Optimal Embedment of Concrete-Filled Circular FRP Tubes into Concrete…

Article *in* Journal of Engineering Mechanics · April 2010

DOI: 10.1061/(ASCE)EM.1943-7889.0000091

2 authors:

Pedram Sadeghian
Dalhousie University
23 PUBLICATIONS **66** CITATIONS
SEE PROFILE

Amir Fam
Queen's University
177 PUBLICATIONS **1,804** CITATIONS
SEE PROFILE

BOND-SLIP ANALYTICAL FORMULATION TOWARDS OPTIMAL EMBEDMENT OF CONCRETE-FILLED CIRCULAR FRP TUBES INTO CONCRETE FOOTINGS

Pedram Sadeghian [1] and Amir Fam, M.ASCE [2]

ABSTRACT

This paper presents a robust analytical model for a moment connection of concrete-filled fiber reinforced-polymer (FRP) tubes (CFFTs) to concrete footings. The CFFT connection is based on a simple approach of direct embedment into the footing, thereby eliminating the need for connection rebar or mechanical devices. The CFFT is externally subjected to lateral and axial loads, resembling practical applications such as piles affixed to pile caps, bridge columns or utility poles. The model adopts the concepts of equilibrium, deformations compatibility, and nonlinear concrete stress-strain behavior. It also employs a 'bond stress-slip' relation that can be obtained from simple push-through tests on some of the commercially used tubes. The model can predict the critical embedment length X_{cr}, which is the minimum length required to achieve material failure of the CFFT outside the footing, and bond failure inside the footing, simultaneously. If the actual embedment length is less than X_{cr}, bond failure occurs prematurely, at a lower strength that can also be predicted by the model. The model was verified using experimental data and showed that X_{cr} was only 0.7 the diameter for that case. A sensitivity parametric analysis was carried out and lead to some approximations. Based on which, a simple closed-form expression was established for X_{cr} in the case of lateral loading only.

---

[1] Post-doctoral Fellow, Dept. of Civil Engineering, Queen's University, Kingston, ON, Canada.
[2] Professor and Canada Research Chair in Innovative and Retrofitted Structures, Dept. of Civil Engineering, Queen's University, Kingston, ON, Canada. E-mail: fam@civil.queensu.ca

Keywords: Concrete-filled FRP tube, CFFT, joint, connection, footing, bond, moment, model.

INTRODUCTION

Hybrid construction using innovative systems such as concrete-filled fiber reinforced polymer (FRP) tubes (CFFTs), as cast-in-situ or precast members, offer several advantages (Mirmiran and Shahawy, 1997, and Fam and Rizkalla, 2002). The tube provides a permanent noncorrosive form for the concrete fill, and bi-directional reinforcement at the same time. Unlike steel tubes, the FRP tube laminate can be engineered to provide different mechanical properties in the orthogonal directions (Fam et al., 2003(a)). CFFTs have been used in field applications, including marine piles (Fam et al, 2003(b)) and in a bridge pier (Fam et al., 2003(c)). They also have a strong potential for utility and light pole applications (Qasrawi and Fam, 2008).

Seible et al. (1995) tested two different moment connections of carbon-FRP (CFRP) CFFTs, one with steel bars connecting the CFFT to a reinforced concrete (RC) footing, and the other with the CFFT embedded inside an RC footing to a depth of 1.3 times the diameter. The study showed that the former was more ductile, while the latter had higher flexural strength. Pseudo-ductile plastic hinges have also been proposed, using CFRP dowels that provide ductility through gradual slip between the concrete and the bars (Wernli and Seible, 1998). This ductility, however, is only in one direction, and the deformation and damage are nonreversible.

Zhu et al. (2004) tested three connections of CFFT to RC footings, in 1/6 scale modular piers, namely, a male-female connection, dowel-bars connection with and without CFFT embedment in footing, and post-tensioning of the CFFT to the footing. The study showed that the embedment of the CFFT into the footing provides additional benefit for the connection. Zhu et al. (2006) extended this work by testing CFFT column-footing assemblies to investigate construction feasibility and seismic performance of the joints, for both precast and cast-in-place

CFFTs, in comparison to conventional RC columns. The FRP tube, when secured properly in the footing, showed great influence on the seismic performance of the column by providing both longitudinal reinforcement and hoop confinement to the concrete core.

Recently, Nelson et al. (2008) tested CFFT cantilevered specimens embedded into RC footings at various embedment lengths, without any dowel-bars or post-tensioning. A short embedment of about 0.73 the diameter was sufficient to achieve flexural failure outside the footing. The interfacial bond strength between the CFFT and concrete was also established using push-through tests, and was found to be about 0.7 MPa. Direct embedment of CFFTs without any rebar or mechanical connection greatly simplified and accelerated constructability.

While CFFTs have been studied extensively as structural members, very few studies as was shown, have addressed their connections to other structural members. These few studies were mainly experimental. In this paper, an analytical approach is developed for the connection of CFFT members to RC footings by direct embedment. The CFFT member is subjected to a general state of axial load, bending moment and shear force.

DESCRIPTION OF THE ANALYTICAL MODEL

The objective of the proposed model is to determine the critical embedment length X_{cr} of circular CFFTs into RC footings, to provide a fixed connection, without the use of dowels or any mechanical devices. Figure 1 shows the geometry of the problem under consideration. The CFFT is subjected to a general loading condition comprising transverse and axial loadings at the free end. The general embedment length is X, while the length of CFFT outside of the footing is L, and the outer diameter of tube is D. It is hypothesized that if the embedment length is smaller than the critical value (i.e. $X < X_{cr}$), a premature bond failure of the CFFT will occur within the

RC footing, before the CFFT achieves its full potential strength at a section outside the footing. On the other hand, if $X >> X_{cr}$, although bond failure is avoided, there may be an unnecessarily excessive embedment length.

The model is based on static equilibrium equations and deformations compatibility relationships for the free body diagram of the connection region (Fig. 2). The problem is solved at the ultimate state of bond failure. The external loads acting on the CFFT are reduced to a moment M, a shear force V, and an axial load *P*, acting at the face of the RC footing. The moment and shear are coupled through the moment arm *L* ($M = V.L$).

A summary of the assumptions made in this model can then be listed as follows, in conjunction with Fig. 2:

1. All contact interfaces between the CFFT and RC footing are subjected to bearing stresses in compression, but separation could occur in tension (i.e. adhesion is insignificant).
2. Given the relatively short embedment length expected for most practical cases, only one inflection point exists within the embedment length, with regard to transverse bearings.
3. The bearing compressive stress distribution on concrete follows the nonlinear stress-strain constitutive relationship of concrete in compression (Collins and Mitchell, 1997), in which the compressive stress (σ) corresponding to a strain (ε) is given by:

$$\sigma = f_c' \left[2\frac{\varepsilon}{\varepsilon_{co}'} - \left(\frac{\varepsilon}{\varepsilon_{co}'} \right)^2 \right] \qquad (1)$$

   where f_c' is the concrete compressive strength and ε_{co}' is the corresponding strain.

4. 'Bond stress-slip' response is dominant in the tension region only, below neutral axis (i.e. the bond (shear) stresses, which is a resistance factor against bond failure, are applied on the sliding interface in the tension region).

5. Slip at the beginning and the end of the CFFT embedment length, longitudinally, is equal (i.e. $S_{x=x_1} = S_{x=-x_2}$), given its relatively short length.
6. Slip distribution in the tension region, transversely, is linear with a zero value at neutral axis.
7. Strains in the two orthogonal directions of the embedded CFFT segment vary linearly and the equivalent curvatures of the CFFT segment are referred to as α and β.
8. The concrete footing extends sufficiently beyond the end of the CFFT embedment length.

General Expressions for Internal Forces

Figure 2 shows the resistance stress distributions, and their resultant forces, acting on the connection region of the CFFT, under the external forces V, M, and P. Two systems contributing to the overall resistance of the connection are established: (a) a transverse system comprising the couple produced by the forces F_1 and F_2, which are the resultants of compressive stresses acting on the transverse bearing interfaces; and (b) a longitudinal system comprising the couple produced by the forces F_3, which is the resultant of the compressive stresses acting on the end bearing interface of the circular cross section, and F_4 which is the resultant of shear (bond) stresses acting on the tension side (the sliding interface).

The mathematical expressions of the resistance resultant forces, F_1 to F_4, and the corresponding moments, M_1 to M_4, are presented next. Moments are taken with respect to a reference point located at the intersection of the *y* and *z* axes (Fig. 2). The y-axis is located at the inflection point, at distances x_1 and x_2 from the front and rear ends of the embedment length, respectively, while the *z*-axis is located at the center of the circular cross-section.

$$F_1 = \int_{x=0}^{x=x_1} \int_{\theta=-\pi/2}^{\theta=+\pi/2} \left(\sigma_{r_1} \cos\theta\right) R \, d\theta \, dx \tag{2}$$

$$M_1 = \int_{x=0}^{x=x_1} \int_{\theta=-\pi/2}^{\theta=+\pi/2} x \left(\sigma_{r_1} \cos\theta\right) R \, d\theta \, dx \tag{3}$$

where F_1 and M_1 correspond to the bearing interface with the length x_1. $\sigma_{r_1} = \sigma_{r_1}(\theta, x)$ is the radial compressive bearing stress at a particular point with the coordinates (θ, x) on the cylindrical interface of the length x_1. The distribution of bearing stresses σ_{r_1} in the transverse direction at a general section, at *x*, is shown in Fig. 3. R is the outer radius of the tube.

$$F_2 = \int_{x=0}^{x=-x_2} \int_{\theta=-\pi/2}^{\theta=+\pi/2} \left(\sigma_{r_2} \cos\theta\right) R \, d\theta \, dx \tag{4}$$

$$M_2 = \int_{x=0}^{x=-x_2} \int_{\theta=-\pi/2}^{\theta=+\pi/2} x \left(\sigma_{r_2} \cos\theta\right) R \, d\theta \, dx \tag{5}$$

where F_2 and M_2 correspond to the bearing interface with the length x_2. $\sigma_{r_2} = \sigma_{r_2}(\theta, x)$ is the radial compressive bearing stress at a particular point with the coordinates (θ, x) on the cylindrical interface with the length x_2. As indicated earlier, it is assumed that only one inflection point exists, due to the short embedment length. This is different from the problem of laterally loaded piles embedded in soil, where multiple inflection points may exist along the typically very long embedment length.

$$F_3 = \int_{y=R-x_3}^{y=R} \left(\sigma_x\right) 2\sqrt{R^2 - y^2} \, dy \tag{6}$$

$$M_3 = \int_{y=R-x_3}^{y=R} y \left(\sigma_x\right) 2\sqrt{R^2 - y^2} \, dy \tag{7}$$

where F_3 and M_3 correspond to the end bearing interface and $\sigma_x = \sigma_x(y)$ is the longitudinal compressive bearing stress within the length x_3.

$$F_4 = \int_{x=-x_2}^{x=x_1} \int_{\theta=-(\pi-\phi)}^{\theta=\pi-\phi} (\tau_{rx})\, R\, d\theta\, dx \tag{8}$$

$$M_4 = \int_{x=-x_2}^{x=x_1} \int_{\theta=-(\pi-\phi)}^{\theta=\pi-\phi} R\cos\theta\, (\tau_{rx})\, R\, d\theta\, dx \tag{9}$$

where F_4 and M_4 are the resultant force and corresponding moment along the sliding interface with the length $X = x_1 + x_2$, $\tau_{rx} = \tau_{rx}(\theta, x)$ is the shear (bond) stress along the sliding interface, and ϕ is the angle to the end of the perimeter of the region in compression (Fig. 2).

Reduced Forms for Internal Forces and Equilibrium

In order to solve the above integrals, the stress distribution functions are required. Figure 3 shows that the radial bearing stress $\sigma_r = \sigma_r(\theta, x)$ at a general section is decreased from the maximum value of $\sigma_{r_m}(x)$ to zero, when θ is increased from zero to $\pm\pi/2$ based on the following relationship:

$$\sigma_r(\theta, x) = \sigma_{r_m}(x)\left(1 - \frac{2\theta}{\pi}\right) \quad , \quad 0 \le \theta \le \frac{\pi}{2} \tag{10}$$

On the other hand, based on Eq. (1) of the concrete constitutive relationship in compression and the linear strain distribution assumed longitudinally ($\varepsilon_y = \alpha\, x$) (Fig. 2), the maximum value of the radial stress $\sigma_{r_m}(x)$ is expressed as follows:

$$\sigma_{r_m}(x) = f_c'\left[2\frac{\alpha\, x}{\varepsilon_{co}'} - \left(\frac{\alpha\, x}{\varepsilon_{co}'}\right)^2\right] \tag{11}$$

As such, F_1 and M_1 given in Eqs. (2) and (3) can be expressed as follows:

$$F_1 = 2\int_{x=0}^{x=x_1}\int_{\theta=0}^{\theta=\frac{\pi}{2}} f_c'\left[2\frac{\alpha\, x}{\varepsilon_{co}'} - \left(\frac{\alpha\, x}{\varepsilon_{co}'}\right)^2\right]\left(1-\frac{2\theta}{\pi}\right)\cos\theta\, R\, d\theta\, dx \tag{12}$$

$$M_1 = 2\int_{x=0}^{x=x_1}\int_{\theta=0}^{\theta=\frac{\pi}{2}} x\, f_c'\left[2\frac{\alpha\, x}{\varepsilon_{co}'} - \left(\frac{\alpha\, x}{\varepsilon_{co}'}\right)^2\right]\left(1-\frac{2\theta}{\pi}\right)\cos\theta\, R\, d\theta\, dx \tag{13}$$

The integrals are then reduced to the following expressions:

$$F_1 = \frac{4R}{\pi}\, f_c'\left[\frac{\alpha\, x_1^2}{\varepsilon_{co}'} - \frac{\alpha^2 x_1^3}{3\varepsilon_{co}'^2}\right] \tag{14}$$

$$M_1 = \frac{4R}{\pi}\, f_c'\left[\frac{2\alpha\, x_1^3}{3\varepsilon_{co}'} - \frac{\alpha^2 x_1^4}{4\varepsilon_{co}'^2}\right] \tag{15}$$

Similarly, F_2 and M_2 given in Eqs. (4) and (5) are reduced to the following expressions:

$$F_2 = \frac{4R}{\pi}\, f_c'\left[\frac{\alpha\, x_2^2}{\varepsilon_{co}'} - \frac{\alpha^2 x_2^3}{3\varepsilon_{co}'^2}\right] \tag{16}$$

$$M_2 = \frac{4R}{\pi}\, f_c'\left[\frac{2\alpha\, x_2^3}{3\varepsilon_{co}'} - \frac{\alpha^2 x_2^4}{4\varepsilon_{co}'^2}\right] \tag{17}$$

As shown in Fig. 2, and based on linear strain distribution in the transverse direction at the end interface $\left(\varepsilon_x = \beta\left(y - R + x_3\right)\right)$, as well as the parabolic bearing stress distribution (Eq. 1), F_3 and M_3 given in Eqs. (6) and (7) can be expressed as follows:

$$F_3 = \int_{y=R-x_3}^{y=R} 2\, f_c'\left[2\frac{\beta\left(y+x_3-R\right)}{\varepsilon_{co}'} - \left(\frac{\beta\left(y+x_3-R\right)}{\varepsilon_{co}'}\right)^2\right]\sqrt{R^2-y^2}\; dy \tag{18}$$

$$M_3 = \int_{y=R-x_3}^{y=R} 2y\, f_c'\left[2\frac{\beta\left(y+x_3-R\right)}{\varepsilon_{co}'} - \left(\frac{\beta\left(y+x_3-R\right)}{\varepsilon_{co}'}\right)^2\right]\sqrt{R^2-y^2}\; dy \tag{19}$$

These integrals are then reduced to the following expressions:

$$F_3 = \frac{2\beta^2 f_c'}{\varepsilon_{co}'^{\,2}}\left[(x_3 - R)\left(2\frac{\varepsilon_{co}'}{\beta} + x_3 - R\right)A + 2\left(\frac{\varepsilon_{co}'}{\beta} + x_3 - R\right)B - C\right] \tag{20}$$

$$M_3 = \frac{2\beta^2 f_c'}{\varepsilon_{co}'^{\,2}}\left[(x_3 - R)\left(2\frac{\varepsilon_{co}'}{\beta} + x_3 - R\right)B + 2\left(\frac{\varepsilon_{co}'}{\beta} + x_3 - R\right)C - D\right] \tag{21}$$

where, $A = \frac{\pi R^2}{4} - \frac{R - x_3}{2}\sqrt{2Rx_3 - x_3^2} - \frac{R^2}{2}\arcsin\left(\frac{R - x_3}{R}\right)$, $B = \frac{1}{3}\sqrt{\left(2Rx_3 - x_3^2\right)^3}$,

$C = \frac{\pi R^4}{16} - \frac{R^2(R - x_3)}{8}\sqrt{2Rx_3 - x_3^2} + \frac{R - x_3}{4}\sqrt{\left(2Rx_3 - x_3^2\right)^3} - \frac{R^4}{8}\arcsin\left(\frac{R - x_3}{R}\right)$, and

$D = \frac{3x_3(x_3 - 2R) + 5R^2}{15}\sqrt{\left(2Rx_3 - x_3^2\right)^3}$

In order to establish reduced expressions for F_4 and M_4 given in Eqs. (8) and (9), the 'bond stress-slip' relationship is required. Figure 4 shows this relationship for 'push-through' specimens comprising CFFT stubs embedded in concrete blocks (Nelson et al., 2008). The figure shows that the initial part of the response is fairly linear, until the peak value of bond strength τ_{max} is reached. Based on this observation and the assumed linear variation of slip transversely, below neutral axis, the shear stress distribution $\tau_{rx} = \tau_{rx}(\theta, x)$ on the sliding interface also varies linearly in the transverse direction (Eq. (22)), from zero at $y = R - x_3$ to the maximum value τ_{max} at $y = -R$ (or as θ is reduced from ($\pi - \phi$) to zero, where θ is measured from the extreme tension point on *y*-axis).

$$\tau_{rx} = \tau_{max}\left(\frac{R(1 + \cos\theta) - x_3}{2R - x_3}\right), \quad 0 \le \theta \le \pi - \phi, \quad \phi = \arccos\left(1 - \frac{x_3}{R}\right) \tag{22}$$

As a result, F_4 and M_4 can be expressed in the following expressions:

$$F_4 = 2\int_{x=-x_2}^{x=x_1}\int_{\theta=0}^{\theta=\pi-\phi} \tau_{max}\left(\frac{R(1 + \cos\theta) - x_3}{2R - x_3}\right) R\, d\theta\, dx \tag{23}$$

$$M_4 = 2\int_{x=-x_2}^{x=x_1}\int_{\theta=0}^{\theta=\pi-\phi} R\cos\theta\ \tau_{max}\left(\frac{R\left(1+\cos\theta\right)-x_3}{2R-x_3}\right) R\,d\theta\,dx \tag{24}$$

These integrals are then reduced to the following expressions:

$$F_4 = \frac{2R\left(x_1+x_2\right)\tau_{max}}{2R-x_3}\left(R\sin\phi+\left(R-x_3\right)\left(\pi-\phi\right)\right) \tag{25}$$

$$M_4 = \frac{2R^2\left(x_1+x_2\right)\tau_{max}}{2R-x_3}\left(\left(R-x_3\right)\sin\phi+\frac{R}{2}\left(\pi-\phi-\frac{1}{2}\sin 2\phi\right)\right) \tag{26}$$

To this end, the internal forces have been expressed in closed-forms in terms of five main parameters, namely x_1, x_2, x_3, α, and β. By applying static equilibrium conditions, considering internal and external forces, as shown in Fig. 2, the following three equations are derived:

$$F_3 - F_4 - P = 0 \tag{27}$$

$$V - F_1 + F_2 = 0 \tag{28}$$

$$M + V.x_1 - M_1 - M_2 - M_3 - M_4 = 0 \tag{29}$$

The three equations are insufficient to obtain all parameters. Two additional equations are required as described next.

Compatibility Relationships

In order to establish the additional equations, the compatibility conditions of deformations at the CFFT-footing interface are used. Initial analyses during model development have shown that the compressive stresses in the transverse bearings are well within the nonlinear range, and hence, the use of the parabolic concrete function (Eq. (1)) is quite important. However, at the longitudinal end bearing, strains were generally small and the concrete stress remains within the

linear range. As such, a closed-form approach based on theory of elasticity is used to apply the compatibility conditions at the end bearing interface.

A typical longitudinal section of the footing is illustrated in Fig. 5. The strain and displacement profiles and the bearing stress distribution as well as its corresponding resultant force F_3 at the end interface (section A-A), are also shown. An equivalent circular disk of a radius c, with a uniform stress distribution of intensity q, is used to substitute the original bearing stress system, such that three conditions are satisfied:

(a) the resultants of both systems must be equal (F_3),

(b) the location of both resultants is the same, at a distance $\bar{x}$ from neutral axis:

$$\bar{x} = \frac{M_3}{F_3} - (R - x_3), \text{ and} \tag{30}$$

(c) the radius of the fictitious disc c is established such that the area of the disk is equal to the actual end bearing area (the part of the circular cross-section of the CFFT), which gives:

$$c = \sqrt{\frac{2}{\pi} \int_{R-x_3}^{R} \sqrt{R^2 - y^2}\, dy} \tag{31}$$

This integral is then reduced to the following expression:

$$c = \sqrt{\frac{R^2}{2} - \frac{R - x_3}{\pi} \sqrt{2Rx_3 - x_3^2} - \frac{R^2}{\pi} arcsin\left(\frac{R - x_3}{R}\right)} \tag{32}$$

The displacement distribution $w = w(z')$ under the equivalent disk load, as a function of the depth z' within the concrete footing, can be established based on a three dimensional half-space domain. Analysis has shown that the depth of typical conventional footings is sufficient for using the half-space domain assumption. The maximum displacement $w_m\,(z' = 0)$ at the end bearing interface (i.e. section A-A in Fig. 5, $z' = 0$) is given in Eq. (33), based on the classical theory of elasticity (Timoshenko and Goodier, 1970).

$$w_m = \frac{2\left(1-\nu^2\right)F_3}{\pi E_c\ c} \tag{33}$$

where ν and E_c are Poisson's ratio and elastic modulus of the concrete footing, respectively. Based on the linear displacement profile at the interface, section (A-A) in Fig. 5, the following displacement compatibility relationship is established:

$$w_m = S_u\left(\frac{\bar{x}}{2R-x_3}\right) \tag{34}$$

where S_u is the slip when maximum bond strength is reached and bond failure occurs (this will be discussed in detail in the next section). From Eqs. (33) and (34) the following expression for x_3 can be established:

$$x_3 = 2R - \left[\frac{\left(\pi\, c\, \bar{x}\right)E_c}{2\left(1-\nu^2\right)F_3}\right]S_u \tag{35}$$

The normal strain distribution $\varepsilon = \varepsilon\left(z'\right)$ within the half-space domain under the equivalent disk load has been derived from the general displacement distribution function $w = w\left(z'\right)$, which is reduced to the following expression for the maximum strain $\varepsilon_m\,(z'=0)$ that occurs at the end bearing interface (i.e. section A-A in Fig. 5, $z'=0$):

$$\varepsilon_m = \frac{(1-2\nu)(1+\nu)F_3}{\pi\, c^2 E_c} \tag{36}$$

Based on the linear strain profile in Fig. 5, which indicates that $\varepsilon_m = \beta\,\bar{x}$, and using Eq. (36), the following expression can be established:

$$\beta = \frac{(1-2\nu)(1+\nu)F_3}{\left(\pi\, c^2 \bar{x}\right)E_c} \tag{37}$$

Equations (35) and (37) are the compatibility equations required in addition to the equilibrium Eqs. (27), (28), and (29), to obtain the five unknown parameters.

'Bond Stress-Slip' Behavior

'Bond stress-slip' response at the interface between the GFRP tube and concrete footing generally depends on the texture of the tube surface, concrete strength, and type of loading. Nelson et al. (2008) conducted six push-through tests on CFFT specimens embedded into concrete blocks under concentric compressive axial loading, to establish the 'bond stress-slip' response for 219 mm diameter CFFTs with commonly used commercial GFRP tubes. The specimens included two groups, with embedment lengths of 200 mm and 400 mm, and each group consisted of three similar specimens. The CFFTs were embedded in 500×500×200 mm blocks in the first group and in 500×500×400 mm blocks in the second group. The concrete strength of the footing was 41 MPa. The 'bond stress-slip' responses were shown earlier in Fig. 4. All responses showed a somewhat linear initial part up to the maximum value of bond strength τ_{max}. Once τ_{max} was achieved, the load dropped significantly and a subsequent residual strength was maintained over a large range of slip. The average maximum bond strength τ_{max} and corresponding slip were 0.71 MPa and 2.1 mm, respectively.

The magnitude of slip at bond failure depends on the nature of loading and is not an absolute general value. This concept is explained in Fig. 6. The case under consideration in this model is different from the push-through specimens in that loading is not concentric, due to the moment. As such, a slip gradient on the sliding interface is expected. Figure 6(a) shows the case of push-through specimens, where τ_{max} is uniform over the entire perimeter. The resultant force in this case $F_{(a)} = \pi D X \tau_{max}$ and the corresponding slip, which is also uniform, is $S_{u(a)} = S_{u(conc.)}$, as

shown in Fig. 6(d). To understand the concept of slip gradient, a hypothetical case (b) is first introduced, showing a linear bond stress distribution along the full depth (Fig. 6(b)). When the maximum bond strength τ_{max} is reached at the extreme point, the resultant force $F_{(b)}$ is the integral of a sine-curve distribution of bond stress over the perimeter (πD), which is $F_{(b)} = 0.5\,\pi\, D\, X\, \tau_{max}$ (i.e. $F_{(b)} = 0.5 F_{(a)}$). From Fig. 6(d), the corresponding maximum slip $S_{u(b)}$ then is $0.5\, S_{u(a)}$. In the case under consideration in the model, however, slip occurs in the tension region, below neutral axis (Fig. 6(c)). In this case, when τ_{max} is reached at the extreme fiber, the corresponding resultant force $F_{(c)}$ is the integral of a sine-curve distribution of bond stress over the part of perimeter in tension ($K\,\pi D$, $K \le 1$). As such, $F_{(c)} = K F_{(b)}$ and from Fig. 6(d), the corresponding maximum slip $S_{u(c)} = K S_{u(b)} = 0.5 K S_{u(a)}$, where K is the ratio of the length of perimeter in tension to full perimeter ($K = (\pi - \phi)/\pi$). $S_{u(c)}$ is the value to be used in Eq. (35).

Procedure of Analysis and Critical Embedment Length

Five equations (27, 28, 29, 35 and 37) have been established to solve for the five unknowns x_1, x_2, x_3, α, and β. The input parameters are the forces acting at the face of the footing, M, V, and P, the tube outer diameter $D = 2R$, concrete strength f'_c, corresponding strain ε'_{co}, concrete Poisson's ratio ν, maximum bond strength τ_{max}, and the corresponding ultimate slip $S_{u(conc.)}$ based on push-through tests. The five equations system can be solved by a trial and error numerical procedure. The main output of the analysis is the embedment length $X = x_1 + x_2$ required to achieve the full bond strength τ_{max}, the curvatures α and β, resultant internal forces F_1 to F_4 and moments M_1 to M_4, and bearing stress distributions on the interfaces.

The critical embedment length X_{cr} can then be defined as the minimum embedment length required to achieve 'material failure' of the CFFT outside the footing, essentially the full potential of the system, simultaneously with a 'bond failure' inside the footing. Material failure of the CFFT could be tension- or compression-controlled, depending on the relative magnitudes of M, P, and V. Models are already available in literature to establish the strength of a CFFT member (for example, Fam et al (2003(a))). If the embedment length $X < X_{cr}$, bond failure occurs before the full potential strength of the CFFT is achieved (i.e. a premature failure).

VERIFICATION OF THE MODEL

The model has been used to predict the strength of five cantilever CFFT specimens embedded into concrete footings at various embedment lengths. The specimens were tested by Nelson et al. (2008) in bending, under lateral loading, to establish the critical embedment length. The specimens, referred to as C1 to C5, consist of 219 mm diameter CFFTs embedded into 500×500×500 mm RC footings at various embedment lengths, namely 66 mm, 110 mm, 154 mm, 220 mm, and 330 mm for specimens C1 to C5, respectively. This provides embedment length-to-diameter ratios of 0.3, 0.5, 0.7, 1.0, and 1.5. The specimens were all laterally loaded to failure at a distance, 1100 mm from the face of the footing. Specimens C4 and C5 had a flexural tension failure just outside the footing, whereas specimens C1, C2, and C3 had a 'bond-slip' failure. Figure 7 shows the data points of the measured ultimate bending moment (and ultimate shear load) of all specimens versus the embedment length-to-diameter ratio (X / D).

The model was used to predict the trend shown in Fig. 7. The input parameters obtained from Nelson et al (2008), except for ε'_{co} and ν which were assumed, are: f'_c = 41 MPa, ε'_{co} = 0.002, ν = 0.2, τ_{max} = 0.71 MPa, $S_{u(conc.)}$ = 2.1 mm. In this study, there was no axial loads (P = 0). The

model was then used to solve for the embedment lengths, for various moments, ranging from zero up to the ultimate moment of the CFFT member. The resulting curve is marked as 'General model' in Fig. 7, and shows good agreement with the experimental data points (C1, C2, and C3) representing bond failure. The ultimate moment increases gradually as the embedment length increases, until it reaches the critical embedment length, beyond which, the flat plateau represents the ultimate strength of the CFFT member. To establish the flat plateau, the model by Fam and Rizkalla (2002) for flexural strength of CFFT member has been adopted, accounting for the effect of shear on the FRP laminate strength through the Tsai-Wu failure criteria (Daniel and Ishai, 1994). This also showed good agreement with the average experimental strength of specimens C4 and C5. The critical embedment length X_{cr} was $0.7D$ in this case.

SENSITIVITY ANALYSIS FOR DIFFERENT PARAMETERS

In order to gain a better understanding of the influence of various parameters in the model, a sensitivity study is carried out by establishing the variation of major parameters with (X/D) ratio (Fig. 8). The variations of α and β are shown in Fig. 8(a). The figure shows that for the most part β is larger than α and as (X/D) decreases, both α and β increase. In the hypothetical case of (X/D) equals zero, α and β approach infinity, whereas if (X/D) is assumed to be infinity, α and β approach zero.

Figure 8(b) shows the variations of x_1, x_2, and x_3 with (X/D). It is noticed that x_1 is slightly greater than x_2. This is consistent with the fact that the force F_1 is greater than F_2 by the shear force V ($F_2 = F_1 - V$). The difference between x_1 and x_2 is little because of the very large difference between the embedment length X and the length of the CFFT member outside the

footing, L, which also makes F_1 (or F_2) significantly larger than V. This fact is also demonstrated in Fig. 8(c), where F_1 and F_2 are very close and F_3 is significantly smaller than either of them. It should be noted that this analysis is demonstrated for a laterally loaded cantilever. If an external longitudinal compression load P was also present, the magnitude of F_3 will be significantly higher. Figure 8(b) shows that (x_1 / X), (x_2 / X), and (x_3 / D) change very little with (X / D). Figure 8(d) shows the variations of slip at failure, S_u and the parameter K with (X / D), which are directly affected by x_3 variation.

A SIMPLIFIED CLOSED-FORM MODEL

A closed-form expression for X_{cr} is established in this section for the case of a long CFFT pole subjected to a lateral load only (i.e. $P = 0$ and hence $F_3 = F_4$). Based on the results of the sensitivity study (Fig. 8), the following approximations can be made, leading to a considerable simplification: $x_3 \cong 0.1D$, which is very small, so F_3 can then be assumed at the edge of the CFFT. Also, $x_1 \cong x_2$, equal to $0.5X$. The sensitivity analysis also indicates that the maximum strains in the transverse direction (αx_1 and αx_2) suggest that f_c' is reached and exceeded. Therefore, an approximate triangular stress distribution with a maximum stress of f_c' is assumed at both sides of the transverse bearing area (Fig. 9). Based on these assumptions, Eqs. (14), (25), and (26) are simplified as follows:

$$F_1 = \frac{D\ X\ f_c'}{2\pi} \tag{38}$$

$$F_4 = \frac{\pi D X\ \tau_{max}}{2} \tag{39}$$

$$M_4 = \frac{\pi D^2 X \tau_{max}}{8} \tag{40}$$

The moment arm of the couple formed by forces F_3 and F_4 is equal to $[0.5D + M_4 / F_4 = 0.75D]$. Based on Fig. 9, Eq. (29) is simplified to the following expression:

$M = F_1\left(\frac{2}{3}X\right) + F_4(0.75D)$, leading to: (41)

$$M = D^3\left[\frac{f_c'}{3\pi}\left(\frac{X}{D}\right)^2 + 0.375\pi\,\tau_{max}\left(\frac{X}{D}\right)\right] \tag{42}$$

From which, the required embedment length X for a given moment, when τ_{max} is achieved, can be given by the following single expression:

$$\frac{X}{D} = 5.55\frac{\tau_{max}}{f_c'}\left(\sqrt{1 + 0.31\frac{f_c'}{\tau_{max}^2}\frac{M}{D^3}} - 1\right) \tag{43}$$

By setting the moment M equal to the flexural strength of the CFFT member, X_{cr} can be obtained. Equation (43) is examined in Fig. 7 (Simplified model (a)), and shows very good agreement with the robust general model and experimental results. Because F_3 is significantly smaller than F_1 and F_2 (Fig. 8(c)), the model can be further simplified by ignoring F_3, rendering Eq. (41) reduced to a compacted expression (Eq. (44)), which is also examined in Fig. 7 (Simplified model (b)) and shows reasonable agreement with the robust general model.

$$\frac{X}{D} = \sqrt{\frac{3\pi M}{D^3 f_c'}} \tag{44}$$

While the simplified models, Eqs. (43) and (44), were developed for a case of lateral loading only, they can be used as a conservative approach to obtain X_{cr} for a CFFT under both lateral and axial load. Axial compressive loads make the connection less sensitive to bond failure.

ANALYSIS OF THE RC SHALLOW FOUNDATION

A procedure is proposed for analysis of the footing, as a shallow foundation, under the internal forces produced by the embedded CFFT segment. In conventional analysis of a footing under axial load and moment, the length (*H*) and width (*B*) of the footing are generally established based on the allowable stress of soil ($q_{max} \leq q_{allowable}$) while the thickness (*t*) and steel reinforcement are designed based on the shear forces and bending moments at critical sections. The difference from conventional footings in this case is that the forces are applied internally, within the embedment length of CFFT (Fig. 10(a)). In this case the soil pressure is established similar to the conventional method (i.e. using the axial load *P* and moment *M*). The forces and moments acting on the critical cross-section, however, namely tensile force T_f, moment M_f, and shear V_f are calculated from the free body diagram in Fig. 10(a)). The thickness (*t*) and steel reinforcement of the critical cross-section can then be designed under these forces (Fig. 10(b)).

SUMMARY AND CONCLUSIONS

A robust analytical method was developed for a moment connection between circular concrete-filled FRP tubular (CFFT) members and reinforced concrete (RC) footings. The connection is based on the simple approach of direct embedment of the CFFT member into the footing for a certain length, and hence do not require the use of dowel bars or any mechanical devices. The CFFT member is subjected to lateral or lateral and axial loads at its free end. This resembles several applications such as utility and light poles, which are typically laterally loaded, and bridge columns and piles connection to pile-caps, which could be axially and laterally loaded.

The model is capable of predicting the critical embedment length X_{cr} of the CFFT member, which is the minimum length required to achieve material failure of the CFFT, outside the footing, and bond failure inside the footing, simultaneously. If the actual embedment length X is less than X_{cr}, bond failure occurs prematurely at a lower capacity, and the model can also predict the reduced strength. If X is larger than X_{cr}, bond failure is avoided.

The model is based on the concepts of equilibrium, deformations compatibility, and the nonlinear concrete stress-strain behavior. The model also employs a 'bond stress-slip' relation which can be obtained from simple push-through tests on some of the commercially used FRP tubes. The model was verified using experimental results and showed good agreement. In this case, it was shown that $X_{cr} = 0.7D$, where D is the CFFT diameter.

A sensitivity analysis of various parameters involved in the model was carried out, and lead to some approximations. Based on which, and for the case of zero axial load, a simple closed-form expression was established for X_{cr}. For embedment length less than X_{cr}, the expression can also predict the reduced moment capacity based on bond failure. The expression could also be used to provide a conservative estimation of X_{cr}, for design purposes, in presence of axial load.

ACKNOWLEDGEMENTS

The authors wish to acknowledge the financial support provided by the Ontario Early Researchers Award Program. The Authors are grateful to Hart Honickman and Yu Ching Lai.

NOTATION

c = radius of equivalent disk stress distribution;
d_i = arm of moment in footing;

D = tube outer diameter;
e = load eccentricity;
E_c = concrete elastic modulus;
F_i = resultant force of interface i;
f_c' = concrete compressive strength;
H = length of footing;
i = code of interface (1, 2, 3, or 4);
K = slip surface factor;
L = length of CFFT at the outside of footing;
M = bending moment;
M_i = resultant moment of interface i;
M_f = moment of footing;
M_u = resistance bending moment of CFFT;
P = compressive axial load;
P_c = compression perimeter of CFFT;
P_o = total perimeter of CFFT;
P_t = tension perimeter of CFFT;
q = intensity of equivalent disk stress distribution;
q_{max} = minimum soil pressure;
q_{mix} = maximum soil pressure;
R = tube outer radius;
r = polar coordinate variable (radius);
S_u = ultimate slip;
S_x = slip at position x;
t = thickness of footing;
$\bar{t}$ = area centre position of footing;
T_f = tension force of footing;
V = shear load;
V_f = shear of footing;
w = displacement distribution along z';
X = embedment length;
X_{cr} = critical embedment length;
X_{opt} = optimum embedment length;
x = longitudinal coordinate variable;
x_i = compression length of interface i;
$\bar{x}$ = effective point of F_3;
y = transverse (shear direction) coordinate variable;
z = transverse coordinate variable;
z' = depth in half space region;
α = lateral interface curvature;

β = circular end interface curvature;
ε = compressive strain;
ε_x = compressive strain along x;
ε_y = compressive strain along y;
ε'_{co} = concrete strength corresponding strain;
ε_m = maximum strain;
ϕ = angle of compression region on end section;
ν = concrete Poisson's ratio;
θ = polar coordinate variable (angle);
σ = compressive stress at strain ε;
σ_{r_i} = radial compressive stress on interface i;
σ_{r_m} = maximum radial compressive stress;
σ_x = normal compressive stress along x;
τ_{rx} = shear stress on sliding interface; and
τ_{max} = maximum bond stress.

REFERENCES

1. Collins, M. P., and Mitchell, D. (1997). Prestressed concrete structures, Response Publications, Canada.

2. Daniel, I. M., and Ishai, O. (1994). Engineering mechanics of composite materials, Oxford University Press, New York.

3. Fam, A. Z., and Rizkalla, S. H. (2002). "Flexural behavior of concrete-filled fiber-reinforced polymer circular tubes." *J. Compos. Constr.*, 6(2), 123–132.

4. Fam, A., Flisak, B., and Rizkalla S. (2003(a)). "Experimental and analytical modeling of concrete-filled fiber-reinforced polymer tubes subjected to combined bending and axial loads." *ACI Struct. J.*, 100(4), 499–509.

5. Fam, A., Greene, R. and Rizkalla, S. (2003(b)) "Field Applications of Concrete-Filled FRP Tubes for Marine Piles", Field Application of FRP Reinforcement: Case Studies, *ACI Special Publication*, SP-215-9:161-180.

6. Fam, A., Pando, M., Filz, G. and Rizkalla, S. (2003(c)) "Precast Composite Piles for the Route 40 Bridge in Virginia Using Concrete-Filled FRP Tubes", *PCI Journal*, 48(3):32-45.

7. Mirmiran, A., and Shahawy, M. (1997). "Behavior of concrete columns confined by fiber composites." *J. Struct. Eng.*, 123(5), 583–590.

8. Nelson, M., Lai, Y. C., and Fam, A. (2008). "Moment connection of concrete-filled fiber reinforced polymer tubes by direct embedment into footings." *Advances Struct. Eng.*, 11(5), 537–547.

9. Qasrawi, Y., and Fam, A. (2008). "Flexural load tests on new spun-cast concrete-filled fiber-reinforced polymer tubular poles." *ACI Struct. J.*, 105(6), 750–759.

10. Seible, F., Burgueno, R., Abdallah, M.G., and Nuismer, R. (1995). "Advanced composite carbon shell system for bridge columns under seismic loads." Proceedings of the National Seismic Conference on Bridges and Highways, San Diego, CA, pp.16, (CD-ROM).

11. Timoshenko, S. P., and Goodier, J. N. (1970). Theory of elasticity, 3rd Ed., McGraw-Hill, Tokyo.

12. Wernli, M., and Seible, F. (1998). "Ductile connections of modular bridge girders made of concrete filled FRP tubes," Proceeding of the 1st International Conference on Composites in Infrastructure ICCI'96, H. Saadatmanesh and M.R. Ehsani eds., Tucson, AZ., Jan., pp. 356–367.

13. Zhu, Z., Ahmad, I., and Mirmiran, A. (2006). "Seismic performance of concrete-filled FRP tube columns for bridge substructure." *J Bridge Eng.*, 11(3), 359–370.

14. Zhu, Z., Mirmiran, A., and Shahawy, M. (2004). "Stay-in-place fiber reinforced polymer forms for precast modular bridge pier system." *J. Compos. Constr.*, 8(6), 560–568.

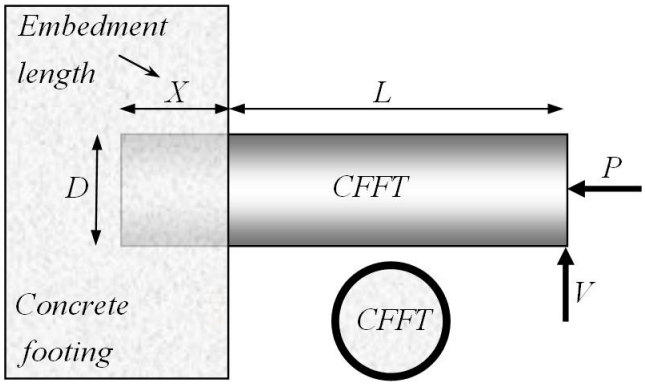

Fig. 1. Geometry of the problem

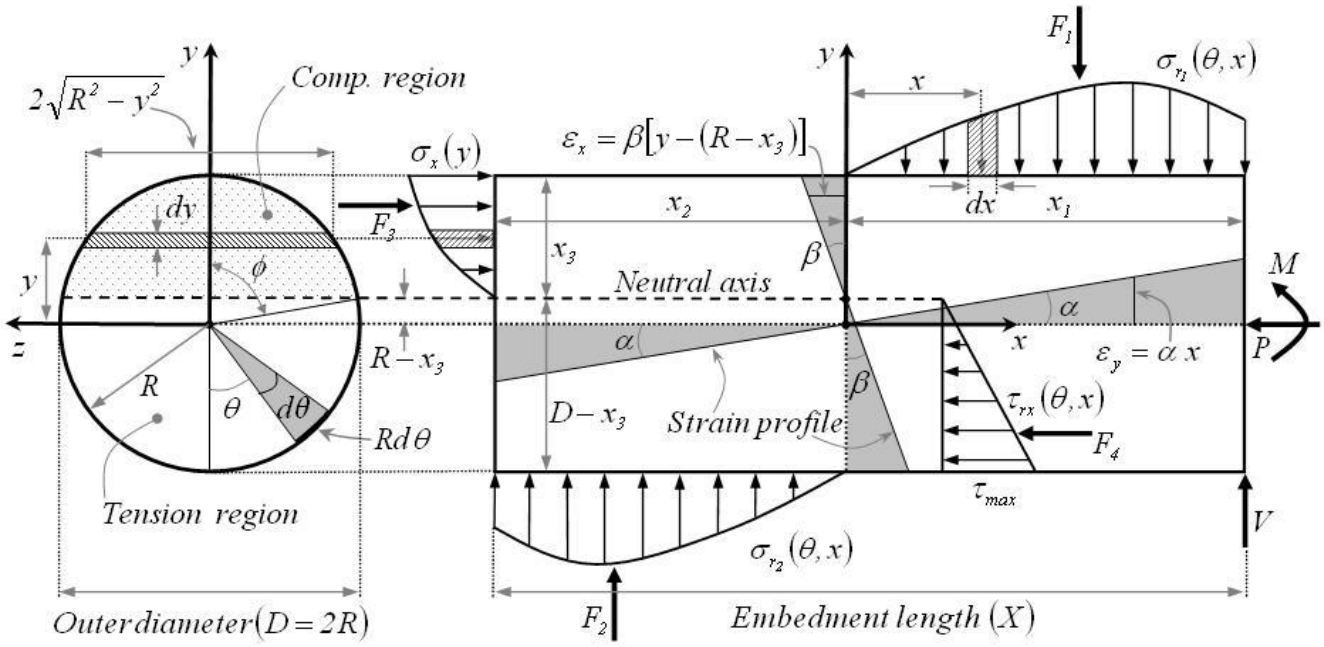

Fig. 2. Internal forces and stress distribution in the longitudinal direction within the embedment length

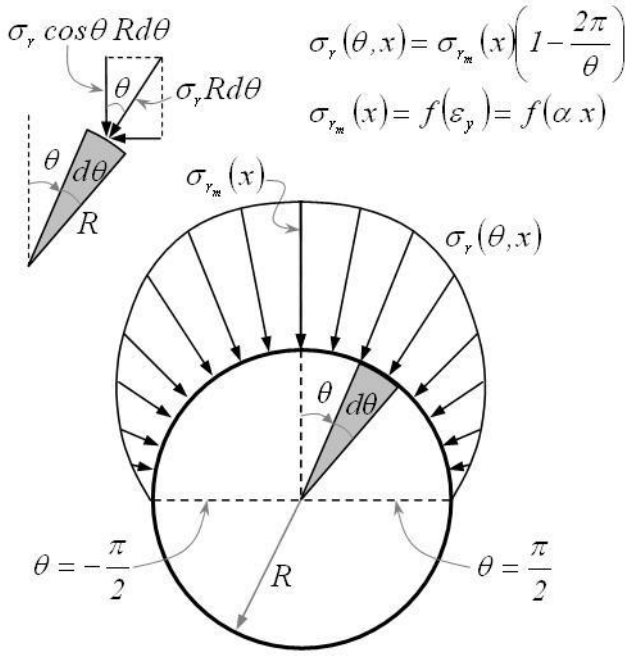

Fig. 3. Lateral stress distribution at a general cross-section within the embedment length

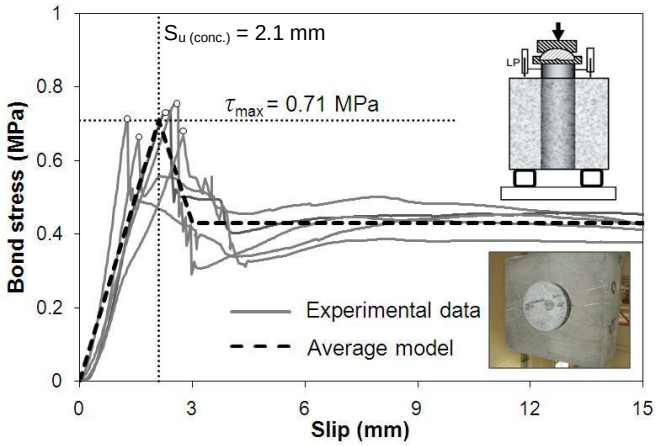

Fig. 4. 'Bond stress-slip' response of CFFT embedded in RC block (adopted from Nelson et al, 2008)

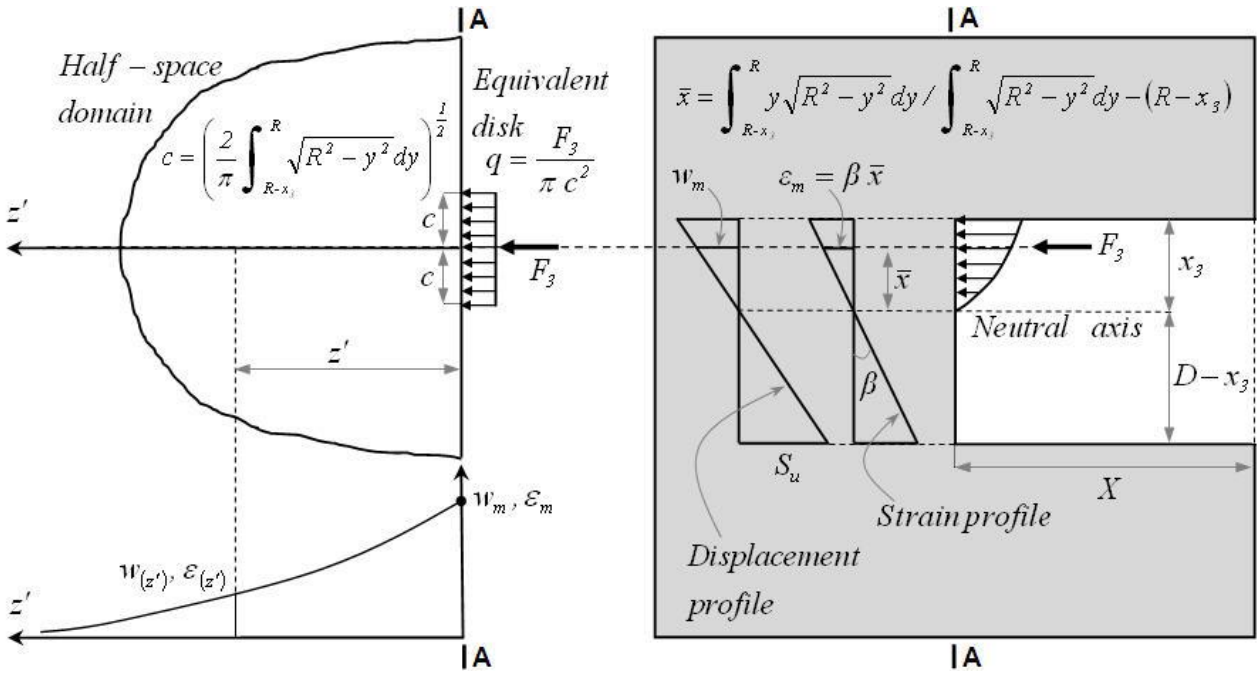

Fig. 5. Stress, strain, and displacement profiles at end interface

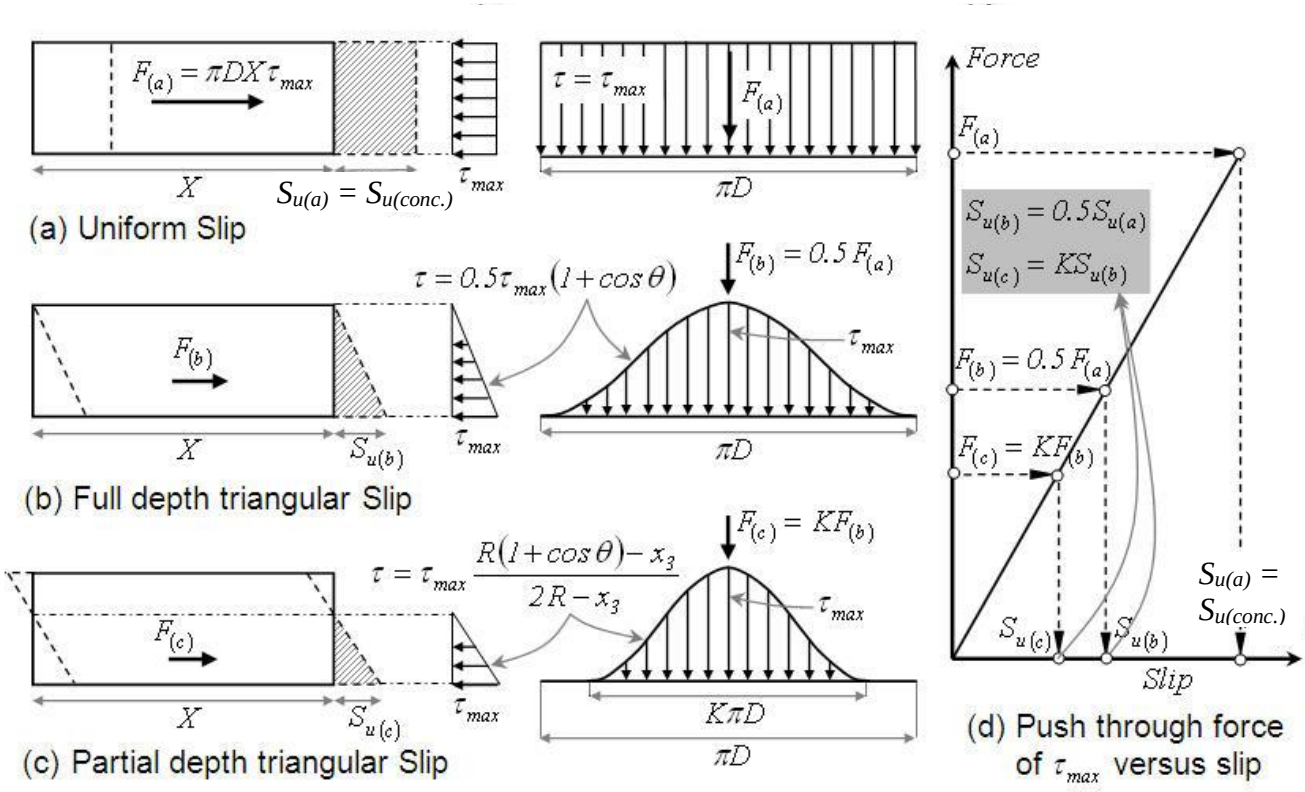

Fig. 6. Simplified slip response

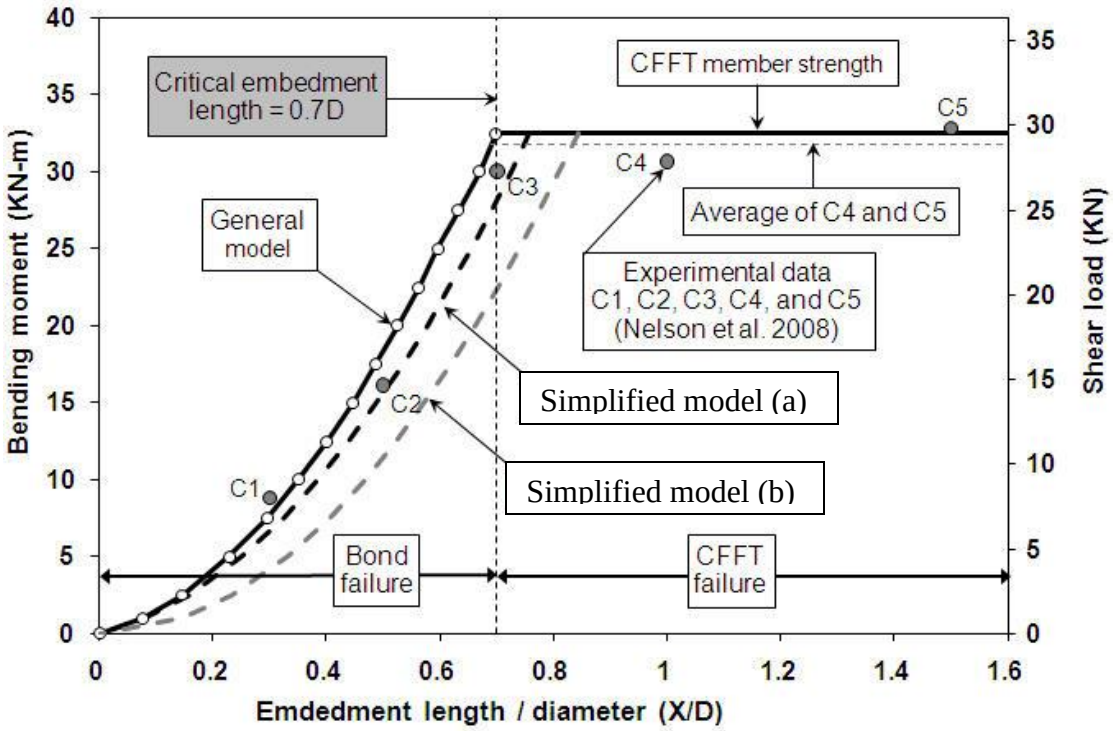

Fig. 7. Experimental and analytical variation of ultimate moment with embedment length

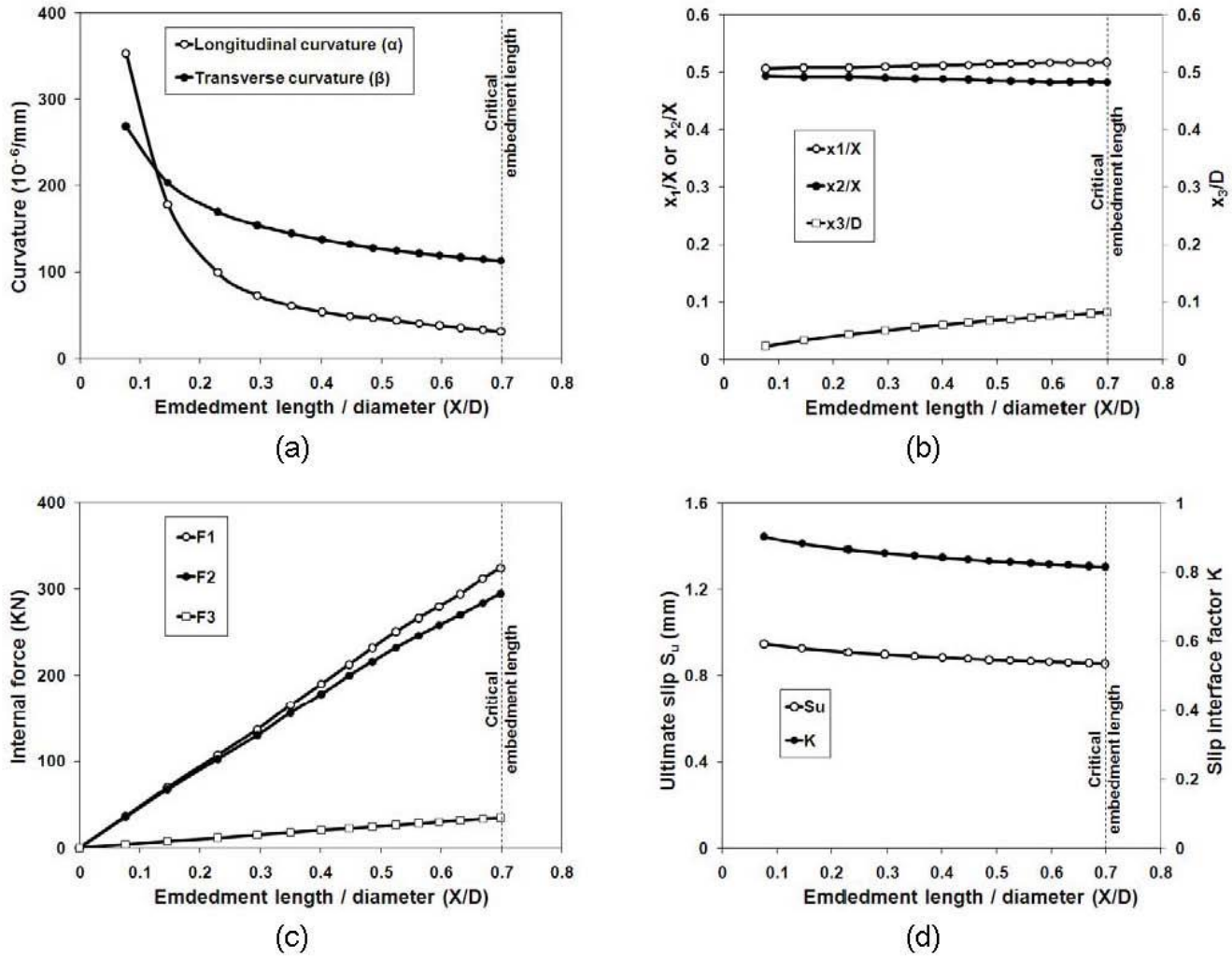

Fig. 8. Summary of the sensitivity analysis

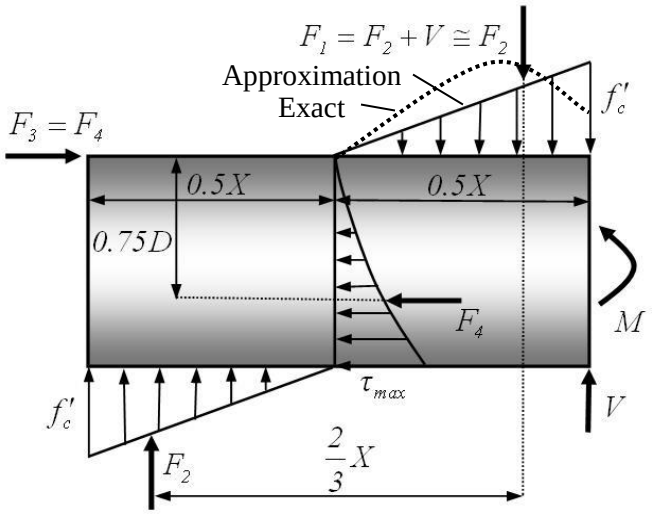

Fig. 9. Geometry and mechanics of the simplified model

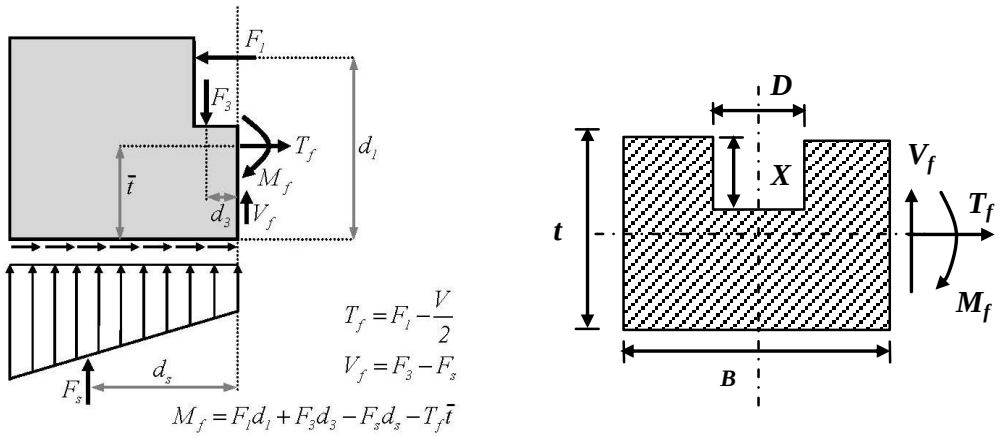

(a) critical section

(b) forces acting on critical cross-section

Fig. 10. Analysis of the RC footing